Science and Technology Indonesia
e-ISSN:2580-4391 *p*-ISSN:2580-4405
Vol. 10, No. 3, July 2025

Research Paper

Corrosion Behavior of Modified F/M Steel with Ti and Dispersed Oxides: Y_2O_3 and ZrO_2 Under High Temperature in Static Liquid Lead

Dhimas Setyo Hadi[1], Hakimul Wafda[2*], Asril Pramutadi Andi Mustari[3], Veri Trisnawan[4,5], Nina Widiawati[2], Fitria Miftasani[2], Djoko Hadi Prajitno[6]

[1]*Bachelor Program of Phyisics Department, Faculty of Mathematics and Natural Science, Institut Teknologi Bandung, Bandung, 40132, Indonesia*
[2]*Research Center for Nuclear Reactor Technology, Research Organization for Nuclear Energy, National Research and Innovation Agency, BJ Habibie Integrated Science Area, South Tangerang, 15310, Indonesia*
[3]*Nuclear Physics and Biophysics Research Division, Physics Department Faculty of Mathematics and Natural Science, Institut Teknologi Bandung, Bandung, 40132, Indonesia*
[4]*Instrumentation and Control, Faculty of Industrial Technology, Institut Teknologi Bandung, Bandung, 40132, Indonesia*
[5]*Research Center for Radiation Process Technology, Research Organization for Nuclear Energy, National Research and Innovation Agency, BJ Habibie Integrated Science Area, South Tangerang, 15310, Indonesia*
[6]*Metallurgical Engineering, Faculty of Manufacturing Technology, Universitas Jenderal Achmad Yani, Bandung, 40285, Indonesia*
*__Corresponding author__: hakimul.wafda@brin.go.id

Abstract
This study investigates the corrosion resistance of Oxide Dispersion Strengthened (ODS) steel in a lead environment, which is crucial for Lead-Cooled Fast Reactors (LFR), a type of Generation IV nuclear reactor. To improve corrosion resistance, two types of oxides-yttrium oxide (Y_2O_3) and zirconium oxide (ZrO_2)-were added individually and in combination to the ODS steel. The samples were synthesized via powder metallurgy and characterized using optical microscopy, X-ray diffraction (XRD), scanning electron microscopy with energy-dispersive X-ray spectroscopy (SEM-EDX), and Vickers hardness testing. Corrosion testing was conducted in static liquid lead at 550°C for 75 hours. The results showed that the addition of Y_2O_3 and ZrO_2 significantly refines grain structure, increases hardness, and promotes the formation of stable, protective oxide layers. Particularly, the dual-oxide (Y_2O_3 + ZrO_2) sample exhibited the most uniform and effective oxide barrier, indicating improved resistance to lead corrosion. These findings demonstrate that dual-oxide dispersion is a promising strategy for improving the durability of structural materials in LFR applications.

Keywords
Corrosion, Lead, ODS Steel, LFR, Oxides

Received: 14 February 2025, Accepted: 24 May 2025
https://doi.org/10.26554/sti.2025.10.3.877-888

1. INTRODUCTION

The most recent generation of nuclear reactors, known as Generation IV, possesses superior qualities compared to previous generations, including enhanced safety, security, sustainability, competitiveness, and adaptability (Bari and Irwanto, 2021). With these advantages, Generation IV nuclear reactors are projected to become a crucial part of the future energy mix in the global effort to reduce carbon emissions and enhance energy efficiency.

The Lead-Cooled Fast Reactor (LFR) is one of the six reactor technologies selected by the Generation IV International Forum (GIF) for further research and development due to its significant potential to address global energy challenges (Lorusso et al., 2018; Wang et al., 2021b). LFR technology offers advantages in safety, non-proliferation, efficiency, and waste management, making it a leading candidate for next-generation nuclear reactors. One of the primary challenges in LFR development lies in the selection and optimization of structural materials, particularly core and cladding materials, which must withstand the high operating temperatures of liquid lead (Pb) and the intense radiation from fast neutrons (Henry and Maloy, 2017; Wang et al., 2021b). Lead's favorable nuclear and physicochemical properties make it a promising coolant for neutron generation in accelerator-driven subcritical systems (ADS) and lead-cooled fast reactors (Alemberti, 2016; Şahin and Wu, 2018). However, cladding materials must resist the corrosive nature of liquid lead while maintaining long-term stability under extreme conditions (Dömstedt et al., 2019; Gong et al., 2022; Wang et al., 2021a). Corrosion control and material compatibility are therefore critical aspects of LFR technology development.

Previous studies have focused on the corrosion behavior

of various structural materials in liquid lead environments. Corrosion phenomena in liquid lead (Pb) environments pose significant challenges for structural and cladding materials due to the aggressive interaction between lead and the material surface (Del Giacco et al., 2012; Xiao et al., 2022). At elevated temperatures, liquid lead can dissolve alloying elements from the material, resulting in the depletion of protective phases and degradation of mechanical properties. Additionally, liquid lead promotes oxidation and can disrupt the formation of stable oxide layers, which are essential for preventing further corrosion. Protective oxide layers, such as Cr_2O_3, Al_2O_3, and Fe_3O_4, have been identified as crucial in mitigating material degradation (Chen et al., 2020; Ricci et al., 2018). However, high-temperature exposure and fast neutron irradiation disrupt these layers, leading to material degradation.

Recent advancements in material science have introduced Oxide Dispersion-Strengthened (ODS) steels as promising candidates for high-temperature nuclear applications, including LFRs (Giuranno et al., 2021; Kimura et al., 2016; Wang et al., 2021a). ODS steels offer several advantages, including increased high-temperature performance, allowing operational limits to reach up to 700°C (Kimura et al., 2016; Wang et al., 2021a; Zinkle et al., 2017). In addition, ODS steels exhibit superior mechanical strength, creep resistance, and radiation tolerance due to their fine-grained structure and dispersed stable oxides like Y_2O_3 and ZrO_2, which contribute to the formation of protective oxide layers (Bassini et al., 2020; Wang et al., 2023; Wafda et al., 2023).

The selection of Y_2O_3 and ZrO_2 as dispersed oxides is based on their unique properties that enhance material stability under extreme conditions. Studies have shown that Y_2O_3 facilitates the crystallization of ZrO_2, leading to the formation of a cubic phase (c-ZrO_2), which is more resistant to structural degradation compared to monoclinic ZrO_2 (Zhu et al., 2023). Despite these advantages, the corrosion rate of ODS steels in liquid metals increases with temperature, and their phase-structural characteristics significantly influence corrosion behavior (Navas and Hernández, 2018). Studies have reported that chromium-containing ODS steels oxidize in lead melts similarly to conventional steels, forming a double-oxide layer (Fe_3O_4/$Fe(Fe_{1-x},Cr_x)_2O_4$), yet the role of dispersed oxides in enhancing corrosion resistance remains unclear (Tsisar and Yeliseyeva, 2007; Yaskiv and Fedirko, 2014).

In previous studies, Y_2O_3 has been widely utilized in ODS steels for its capability to enhance thermal stability and resistance to irradiation by promoting fine and stable oxide particles that hinder dislocation movement (Kimura et al., 2016; Zinkle et al., 2017). On the other hand, ZrO_2 has been investigated for its excellent chemical compatibility with liquid lead and its contribution to forming a dense oxide layer at high temperatures (Bassini et al., 2020; Gong et al., 2022). Zhu et al. (2023) demonstrated that the presence of Y_2O_3 could induce the formation of cubic ZrO_2 (c-ZrO_2), which is more structurally stable than monoclinic ZrO_2 and thus more beneficial in corrosive environments. Comparatively, Jiang et al. (2022) found that coatings containing Y_2O_3 showed improved corrosion resistance against Pb-Bi environments due to better oxide adhesion and reduced element diffusion. While both oxides have shown individual effectiveness, limited studies have examined their combined effect in ODS steels. Therefore, this study aims to fill this gap by comparing the corrosion performance of ODS steels containing Y_2O_3, ZrO_2, and a combination of both under high-temperature static lead conditions. By integrating and extending previous findings, we aim to provide a clearer understanding of how different oxide dispersions influence the corrosion mechanisms in liquid lead environments.

A few researchers have focused on the oxidation behavior of ODS steels in lead-based melts, and there have been limited studies concerned with the long-term stability of these materials under extreme reactor conditions. Despite the known benefits of ODS steels in high-temperature environments, the specific roles of oxides like Y_2O_3 and ZrO_2 in enhancing corrosion resistance under lead exposure are not yet fully understood (Jiang et al., 2022; Wafda et al., 2024). Therefore, this research intends to investigate the corrosion mechanisms of ODS steels in liquid lead environments, particularly focusing on the role of oxide dispersion in mitigating material degradation. The objectives of this research are to evaluate the corrosion resistance of ODS steels, analyze the effects of oxide dispersion on protective layer formation, and provide insights into optimizing structural materials for LFR applications.

Table 1. Nominal Composition of ODS Steel Sample

Fe (%)	Cr (%)	W(%)	Ti(%)	Y_2O_3 (%)	ZrO_2 (%)	Nomenclature
Bal.	9	2	0.35	-	0.35	ODS A
Bal.	9	2	0.2	-	0.2	ODS B
Bal.	9	2	0.2	0.2	0.2	ODS C

2. EXPERIMENTAL SECTION

2.1 Materials

ODS steel samples, consisting of three different compositions as shown in Table 1, were prepared using the powder metallurgy method. High-purity powders were used for mechanical alloying, including Fe (≥99% trace metals basis), Cr (≥99% trace metals basis), W (99.9% trace metals basis), Ti (99.98% trace metals basis), Y_2O_3 (99.99% trace metals basis), and ZrO_2 (99.99% trace metals basis).

2.2 Fabrication Procedure

The powders were mechanically alloyed using a high-energy ball mill by Across International. A total weight of 10 g of powder was loaded into the grinding jar for each milling cycle. The grinding jar used in the process was made of austenitic stainless steel (SS 304). Balls with diameters of 5 mm and 11 mm were used in the mechanical alloying process, and the volume of the grinding jar was 125 ml. The ball-to-powder

ratio (BPR) was 10:1. Milling was conducted for 8 hours at a frequency of 60 Hz at room temperature. A 15-minute break was taken every 30 minutes to cool the powder and maintain room temperature. Following mechanical alloying, the powder was compacted under a load of 100 kg/cm^2 and then sintered in a furnace under an argon gas atmosphere at a temperature of 1200°C for 1 hour, followed by cooling to room temperature. The resulting solid samples had a diameter of 10 mm and a thickness of 2 mm.

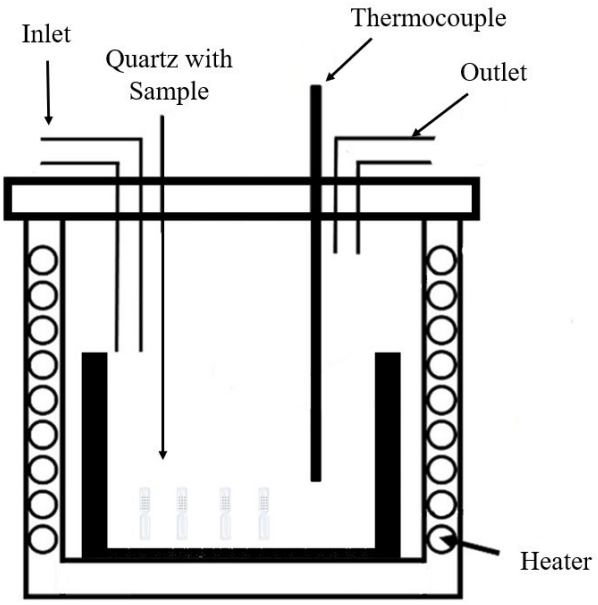

Figure 1. Experimental Setup to Study Corrosion of ODS Steels in Static Pb Environment

2.3 Methods

2.3.1 Corrosion Test

The corrosion testing of the materials in this study was conducted following initial material characterization. The testing was performed in a static Pb environment at a temperature of 550°C for 75 hours, simulating conditions within the operational temperature range of Lead-cooled Fast Reactors (LFR). Thus, the corrosion testing in this experiment simulates the interactions between the Pb-based coolant of LFR reactors and the material. Figure 1 shows a schematic diagram of the autoclave used for the corrosion test, designed to heat samples up to 550°C. The system was equipped with thermocouples to monitor and maintain a consistent temperature throughout the test. The configuration of this autoclave setup is similar to the one used in the study conducted by Martinelli et al. (2020), for high-temperature static Pb-Bi corrosion evaluation. Figure 2 is a schematic of the quartz vessel containing the ODS sample, Pb, and sacrificial Fe metal, which is placed inside the autoclave during testing. The quartz vessel was hourglass shaped with a narrow gap in the center to ensure the ODS sample remained fully submerged in the liquid Pb. Before the corrosion testing,

Figure 2. Quartz Model as a Corrosion Test Vessel for Samples in a Pb Environment

each sample was placed at the bottom of the quartz container to ensure complete immersion in molten Pb. After the test, the quartz container was inverted to allow the sample to separate from the Pb with minimal residual adhesion. Post-test analysis was conducted using SEM-EDS and XRD.

Table 2. Nominal Composition of ODS Steel Sample

Sample	Martensite Area (%)
ODS A	18.860
ODS B	30.600
ODS C	38.107

2.3.2 Characterization

Pre-corrosion Characterization: Prior to corrosion testing, a qualitative phase analysis of the ODS samples was performed using an X-ray diffractometer (XRD, Bruker D8 Advance) with Cu-Kα (α=0.15406 nm) radiation, operating at 40 kV and 40 mA. The morphology and microchemistry of the materials were analyzed using a scanning electron microscope (SEM) (JEOL JSM IT300) operated at 20 kV, equipped with an energy dispersive spectrometer (EDS) detector (Oxford Xmax 20). Additionally, the mechanical properties, such as hardness, were tested using the Vickers microhardness method.

Post-corrosion characterization: After the corrosion tests, the surfaces and prepared cross-sections of the specimens were examined using scanning electron microscopes (SEM) to determine the morphology and dimensional parameters of the formed scales. The elemental composition of the scales and corrosion zones was analyzed using energy dispersive X-ray (EDX) analysis.

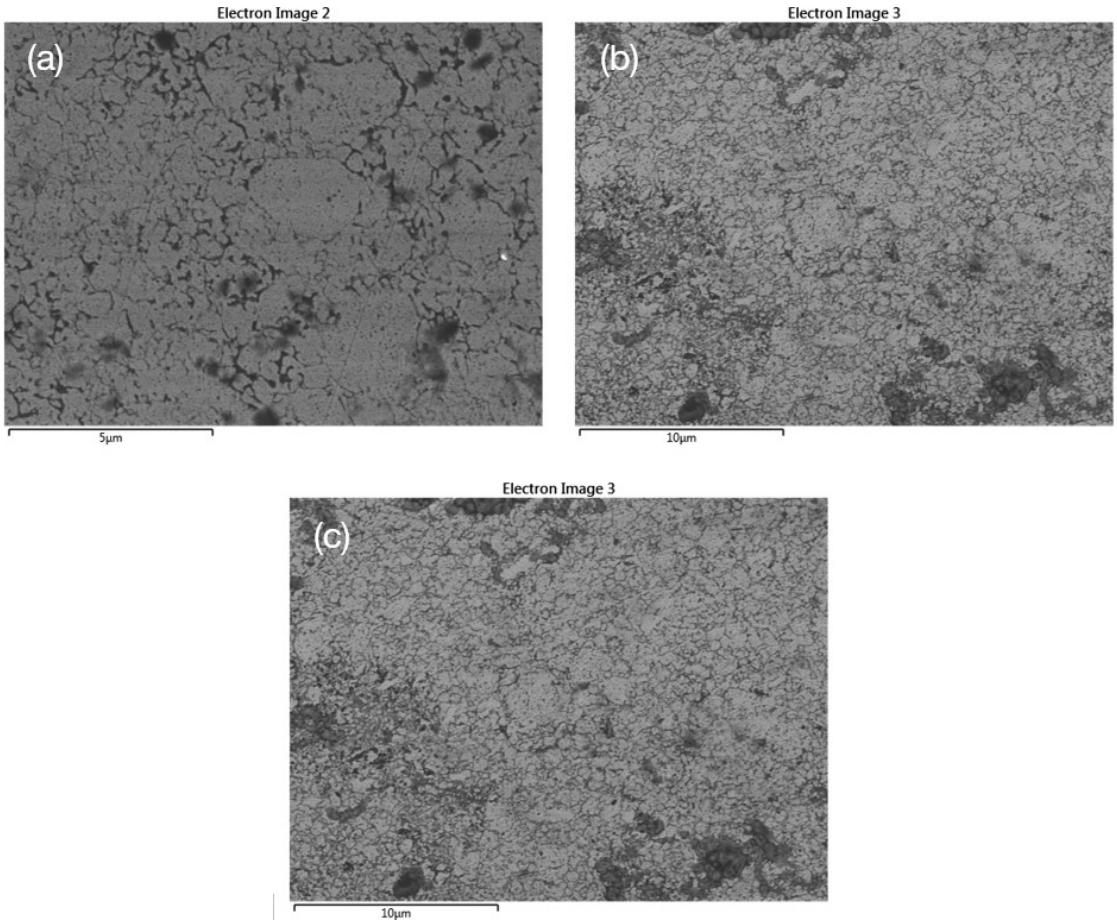

Figure 3. SEM Pre-Oxidize (a) ODS A, (b) ODS B, and (c) ODS C

3. RESULTS AND DISCUSSION

The microstructure of the as-cast ODS samples ODS A, ODS B, and ODS C is shown in Figure 3, revealing the ferritic matrix typical of ODS steel (Parida et al., 2023). In ODS A, surface porosity is evident and spreads throughout the material. These pores, distinguishable by their shape and darker color compared to grains, arise from the consolidation process in powder metallurgy, where voids filled with air form during sintering. The presence of such porosity weakens the mechanical properties, reducing tensile strength and hardness.

The grain structure of ODS A, ODS B and ODS C are illustrated in Figure 3. Grain size is determined by measuring individual grain areas and calculating the average. The results, displayed in Figure 4, indicate that ODS A has an average grain size of 65.296 μm, ODS B has 18.307 μm, and ODS C has 14.384 μm. Additionally, martensite area percentages were analyzed, showing that ODS A contains 18.86% martensite, ODS B 30.6%, and ODS C 38.107%, as presented in Table 2.

XRD analysis as received samples (Figure 5) confirms that all ODS samples exhibit a dominant α-Fe (BCC Fe) phase, characteristic of a ferritic matrix. This aligns with previous studies on 9Cr ODS steel, emphasizing the stability of the ferritic phase due to the absence of austenite stabilizers such as Ni or Mn (Parida et al., 2023). The presence of martensite, as indicated by its increasing percentage from ODS A to ODS C, suggests that variations in processing conditions and composition influence phase transformation and mechanical properties. The ferritic structure remains crucial for high-temperature

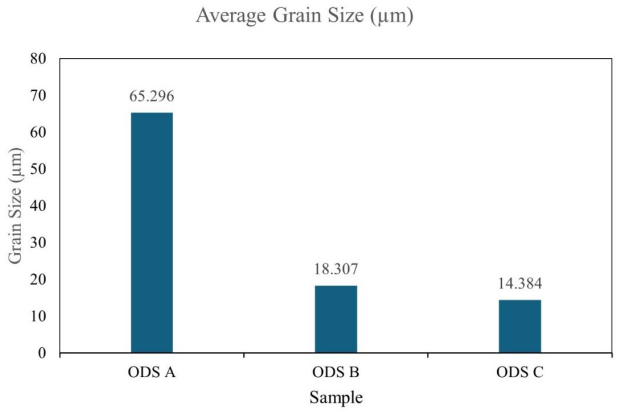

Figure 4. Average Grain Size of the Material

oxidation and corrosion resistance.

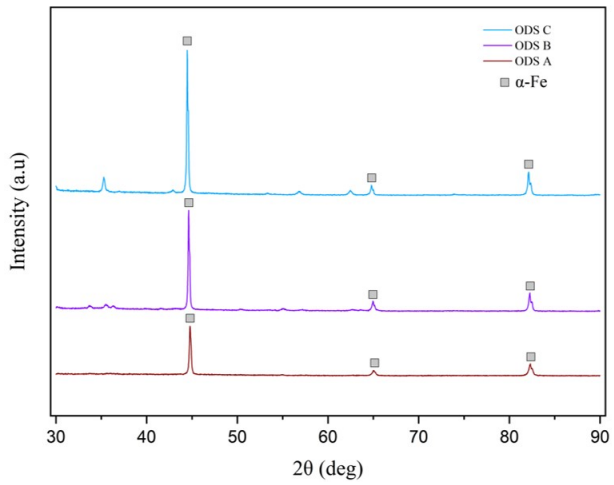

Figure 5. XRD Pre-Oxidized ODS A, ODS B and ODS C

SEM analysis reveals that ODS B retains the same ferritic grain structure as ODS A but with smaller, more uniform grains. Porosity in ODS B is localized, likely due to imperfections in the iso-compaction process. In contrast, ODS C exhibits the smallest and most consistent grain size, suggesting a more optimized iso-compaction process. The addition of both Y_2O_3 and ZrO_2 in ODS C likely contributes to its refined microstructure and improved densification. Although small pores are present, porosity in ODS C is significantly lower than in the other samples.

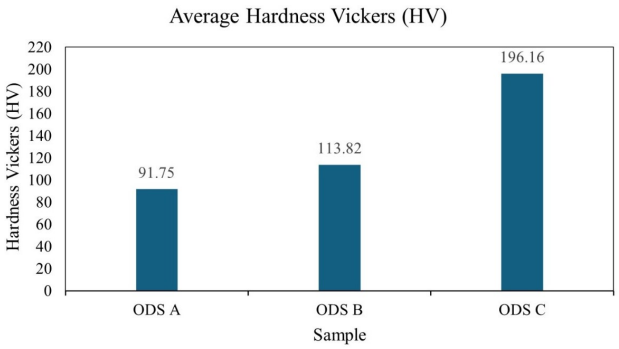

Figure 6. Average Microhardness Vickers of ODS A, ODS B and ODS C

The impact of these microstructural variations on hardness properties is evident in the Vickers hardness results, as shown in Figure 6. The hardness values indicate that ODS A exhibits the lowest hardness (91.75 HV), followed by ODS B (113.82 HV), and ODS C (197.16 HV). This trend correlates with the increase in martensite content and the refinement of grain size. The dominance of the ferritic phase in ODS A leads to lower hardness due to its softer and more ductile nature, whereas ODS C, with the highest martensite percentage and smallest grain size, achieves the highest hardness. These results confirm that grain refinement and martensite fraction significantly enhance hardness, while porosity can contribute to mechanical property degradation. Overall, SEM analysis of all ODS samples confirms the presence of ferritic grains and highlights differences in grain size and porosity. The observed porosity results from the consolidation of powder during iso-compaction, leading to void formation during sintering. This porosity negatively impacts mechanical properties by increasing grain spacing, making the material more susceptible to cracking. Additionally, it influences corrosion resistance by facilitating the penetration of corrosive agents and affects thermal conductivity by altering heat transfer within the material.

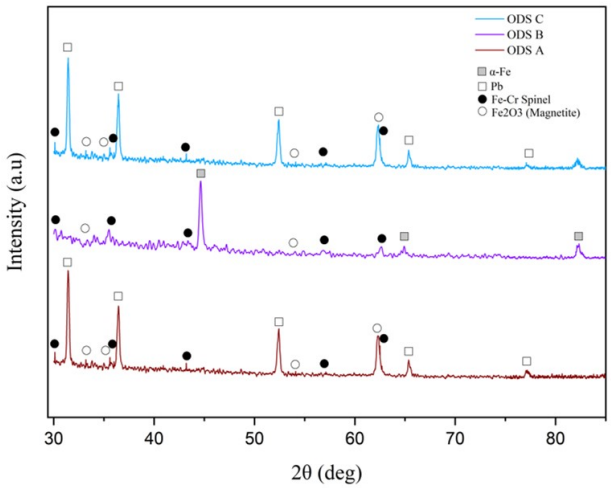

Figure 7. XRD Oxidize ODS A, ODS B and ODS C

The corrosion behavior of ODS A, ODS B, and ODS C in a static liquid Pb environment was examined post-exposure. Following high-temperature exposure in a static Pb environment at 550°C for 75 hours, significant phase transformations were observed. The XRD results after corrosion test in Figure 7 indicate the formation of Fe_2O_3 (magnetite) and Fe-Cr spinel as dominant oxidation products. These findings are consistent with SEM-EDX observations, which revealed the development of a protective oxide scale on the surface of all samples. The oxidation mechanism is attributed to the outward diffusion of Fe and Cr cations through the oxide layer, forming a dual-layered structure consisting of an outer Fe_2O_3-rich layer and an inner Fe-Cr spinel layer (Jiang et al., 2022). Additionally, Pb was also detected in ODS A and ODS C. As shown in the SEM results in Figure 8a Pb layer formed on the outermost surface of ODS A and ODS C, whereas no Pb was observed in ODS B.

Cross-sectional SEM observations of the samples after exposure to pure Pb at 550°C for 75 hours revealed oxidation effects. All samples were covered by solid lead adhering to the surface. Therefore, the exposed specimens were cleaned using a chemical mixture of $CH_3COOH + H_2O_2 + C_2H_5OH$ (1:1:1) at room temperature to remove the Pb. However, some Pb residue remained on certain samples due to excessive thick-

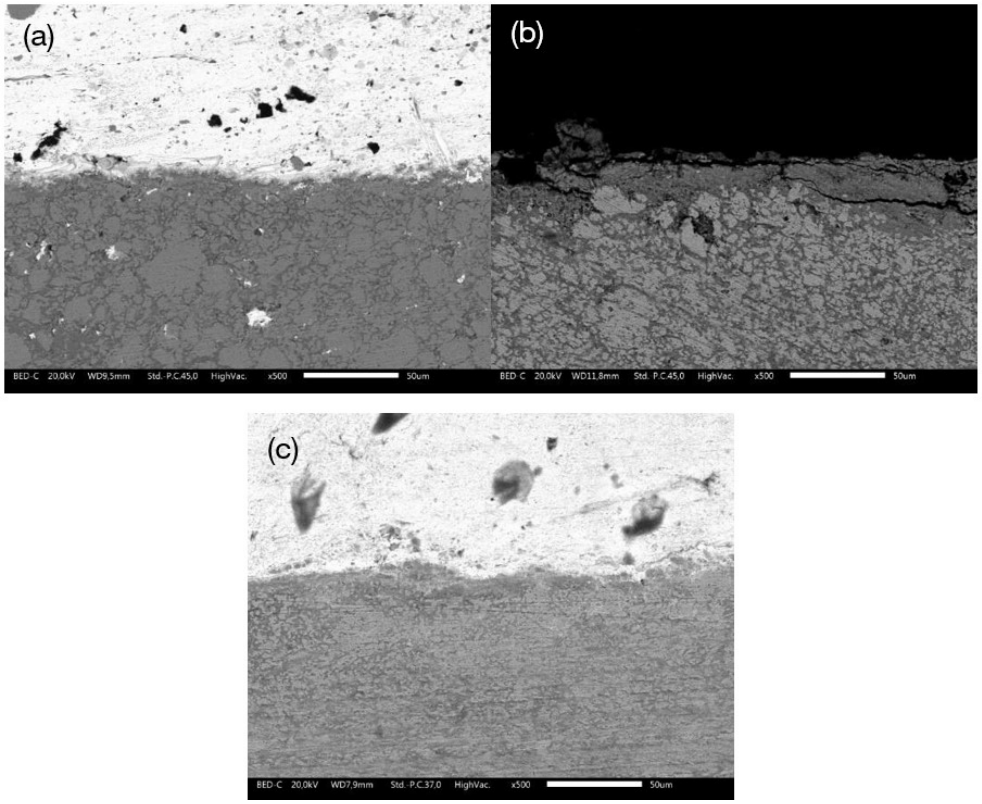

Figure 8. SEM Observations of (a) ODS A, (b) ODS B and (c) ODS C

ness. After exposure, the samples, which were initially shiny and smooth, became dull, indicating corrosion attack by pure Pb. It was determined that the concentration of chromium decreased, particularly in the layer near the surface. The depth of chromium depletion did not exceed a few micrometers. In Figure 8, the structure of the ODS sample is shown, revealing three distinct layers at 500× magnification. The layers observed in the cross-section of the ODS sample consist of a Pb layer, an oxide layer, and a substrate layer. The oxide layer appears as a barrier between the Pb and the substrate, suggesting initial oxidation and chromium depletion. To confirm the composition of each layer formed on the sample EDX mapping and line scan analysis were performed, as shown in Figure 9 and Figure 10, revealing the specific distribution of Pb, oxide phases, and substrate elements across the sample cross-section.

The EDX results shown in Figure 9a reveal the types of layers formed in the structure of ODS A. A high concentration of lead (Pb) is detected on the uppermost surface, indicating is the formation of a Pb layer that has partially reacted with the material. The oxygen (O) element is concentrated within a specific region, signifying the oxide layer formed to protect the material in a high-temperature Pb environment. The primary constituents, iron (Fe) and chromium (Cr), exhibit highly bright areas, indicating regions with high concentrations of these elements. These bright areas correspond to the substrate, which has not reacted with Pb. Pb penetration is minimal, as evidenced by the low Pb content in both the oxide layer and the substrate. This finding demonstrates that the oxide layer effectively protects the substrate from Pb penetration during the corrosion test. The EDX linescan results are presented in Figure 10, are used to further characterize the compositional gradient and confirm layer boundaries within the structure.

Figure 9b displays EDX results for ODS B, indicating the presence of a thin oxide layer that can protect the sample from Pb penetration. Analyzing the Pb element in the EDX results for ODS B reveals several points where Pb is present on the material surface. However, these points do not indicate Pb penetration, as penetration typically occurs in areas with numerous points. Therefore, the Pb observed on the surface of ODS B is assumed to be residual Pb remaining after the material cleaning process. Similarly, Figure 9c displays the EDX results for ODS C. The EDX analysis shows a high O content in the outermost layer of the sample, indicating that this layer is an oxide layer formed during the corrosion test. The Fe and Cr content in the oxide layer is lower than in the substrate layer. This is because the substrate layer does not directly react with Pb during the corrosion test. When examining the Pb content in the material structure, some Pb appears to have entered the material. However, this is believed to be residual Pb remaining after the cleaning process. This is suggested by the inconsistency in the Pb content, with very high Pb levels found in the middle of the material, which differs from the typical Pb

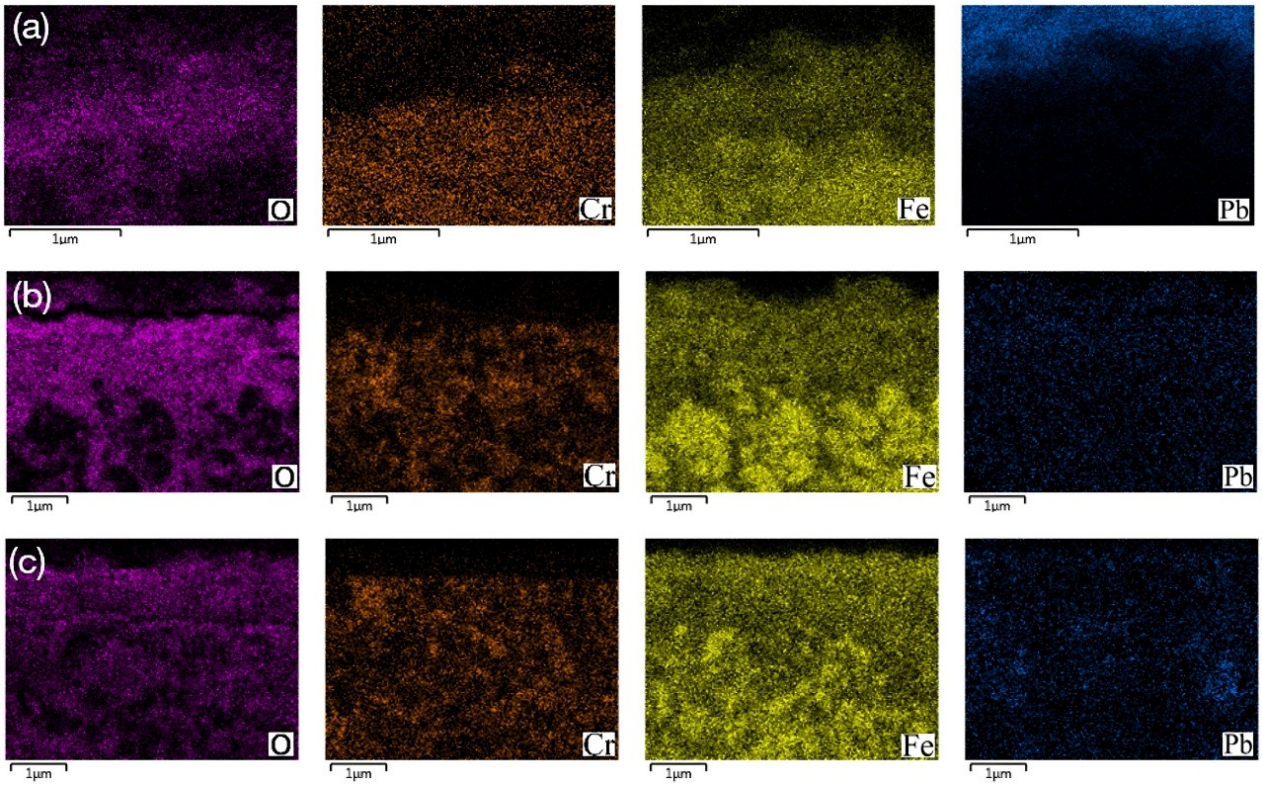

Figure 9. EDS-Mapping Observations of (a) ODS A, (b) ODS B, and (c) ODS C

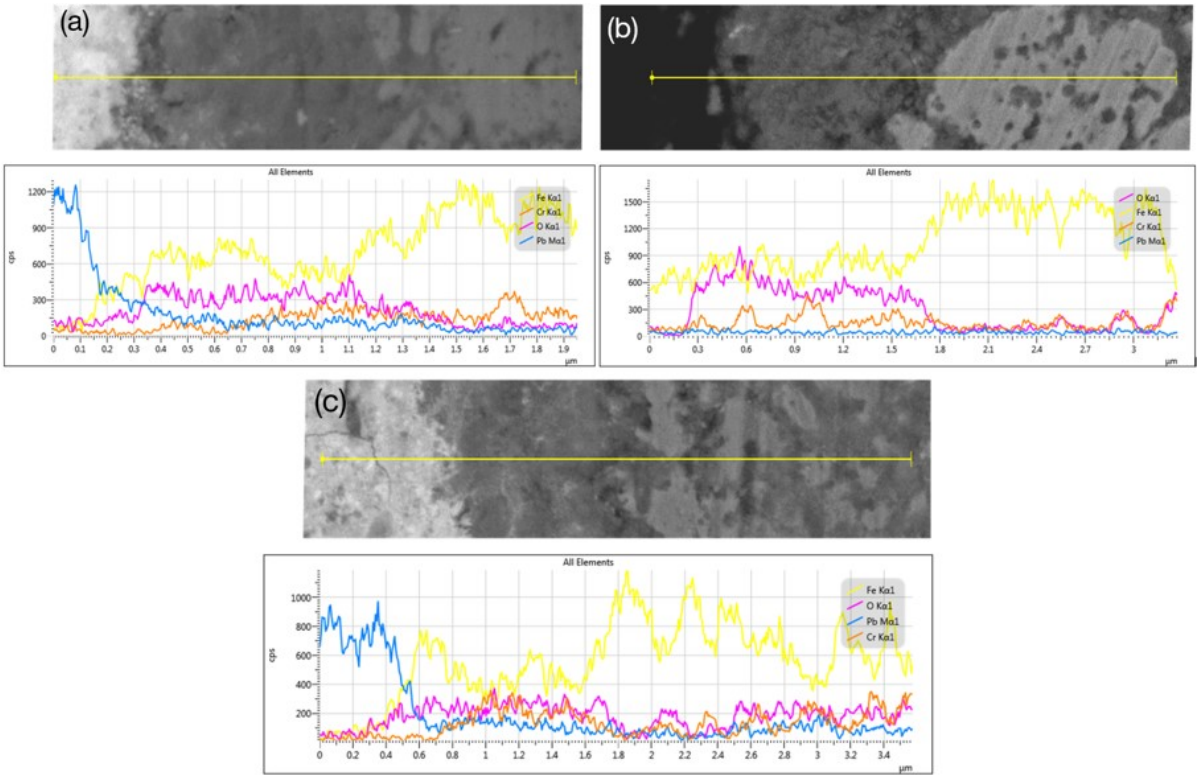

Figure 10. EDS-Line Analysis of (a) ODS A, (b) ODS B, and (c) ODS C

penetration mechanism. Pb penetration usually starts at the outer surface and progresses inward. These findings suggest that the oxide layers formed on ODS B and C effectively protect the substrates from Pb corrosion. Thus, if Pb penetration had occurred, the EDX results should show high Pb content on the outer surface of the substrate. To confirm the types of layers formed in the material's structure, EDX linescan results were used.

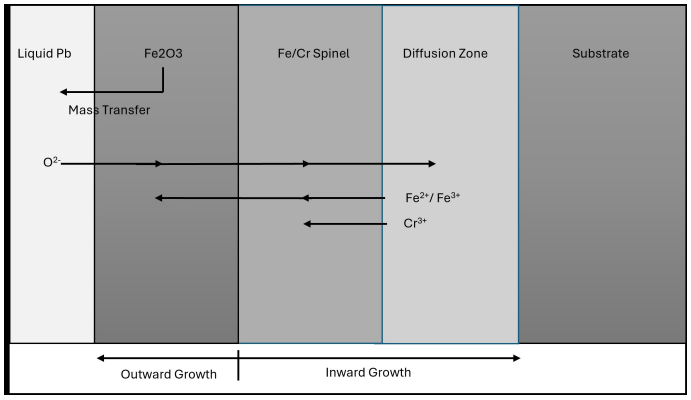

Figure 11. Corrosion Mechanism of F/M Steel in Pb Environment

Table 3. Average Oxide Thickness Value for Each Sample Variation

Sample	AVG (μm)	STDEV
ODS A	7.743	2.2426
ODS B	13.754	2.7115
ODS C	9.189	1.3351

The results of the linescan for sample ODS A are depicted in Figure 10a. The oxide layer is indicated by the elevated oxygen content in a specific area, as illustrated by the purple line in Figure 10a. The substrate layer is characterized by the highest Fe content, which has not reacted with Pb at elevated temperatures. Analyzing the oxygen (O) element reveals a significant increase in thickness, suggesting the formation of an oxide layer on the outer surface of ODS A. To determine the type of oxide formed in this layer, the elements Fe and Cr were examined within this thickness range. The Fe element exhibits a marked increase in the oxide region up to a thickness of 8.1 μm before showing another increase that denotes the substrate area. Therefore, it is inferred that the oxide formed within the thickness range of 3.57 μm to 8.1 μm is Fe_3O_4. The Cr element, on the other hand, shows a significant increase from a thickness of 8.1 µm to 16.3 μm, followed by another rise indicating the substrate area. Within the range of 8.1 μm to 16.2 μm, both Fe and Cr exhibit high concentrations, suggesting the formation of a FeCr layer. Figure 8a presents the assumed types of layers formed in ODS A. Figure 10b. presents the linescan results for each element in ODS B, which are utilized to analyze the oxide layer formed in the sample's structure. Initially, we consider the oxygen (O) element to delineate the oxide layer region. The linescan data reveal a significant increase in oxygen content at a depth of 2.9 μm, followed by a substantial decrease at 16.9 μm. Consequently, the oxide layer is determined to be within the depth range of 2.9 μm to 16.9 μm. Chromium (Cr) exhibits a notable increase from a depth of 3.1 μm up to 17.8 μm. Within this interval, the iron (Fe) particle concentration remains relatively stable until it significantly rises at a depth of 18.3 μm, marking the commencement of the substrate layer in Sample Variation II. The high Cr content and the stable Fe particles within the 3.1 μm to 17.8 μm depth range suggest the formation of a single type of oxide layer in ODS B. Figure 10c. illustrates the linescan results for each element in ODS C. The data reveal a significant increase in oxygen content within the depth range of 4.86 μm to 17.4 μm, indicating that this range represents the oxide layer formed during the corrosion test. Additionally, an increase in oxygen content is observed in the substrate area, attributed to the presence of porosity in the surface structure of ODS C. These pores, being empty spaces, are susceptible to being filled by various elements. However, if these pores are not adequately filled by protective elements, the material becomes more susceptible to lead penetration, which could accelerate corrosion rates.

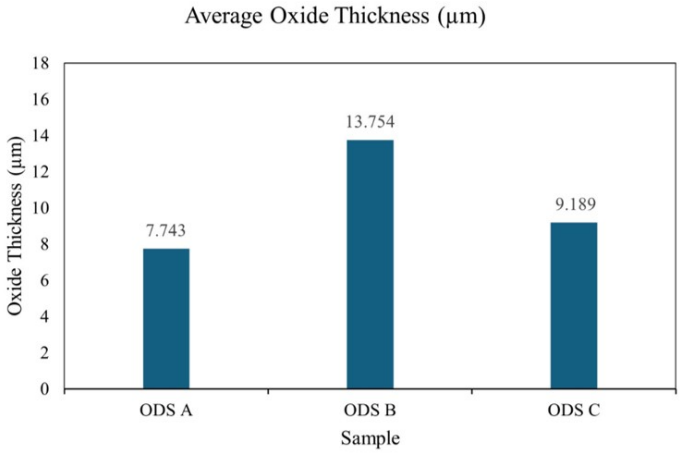

Figure 12. Average Oxide Thickness of ODS A, ODS B, and ODS C after corrosion test under Pb Environment

In corrosion testing experiments, if these pores are not filled with protective elements, the likelihood of lead (Pb) penetration into the sample increases. The linescan results for Sample Variation IV indicate that the pores formed during the synthesis process were filled with oxides during the corrosion test, which is beneficial as the presence of oxides in the pores enhances the material's resistance to corrosion. Within the oxide layer of ODS C, two distinct layers are identified. The first layer, rich in Fe, likely consists of Fe_3O_4, formed within the depth range of 6.2 μm to 12.1 μm. The second oxide layer, within

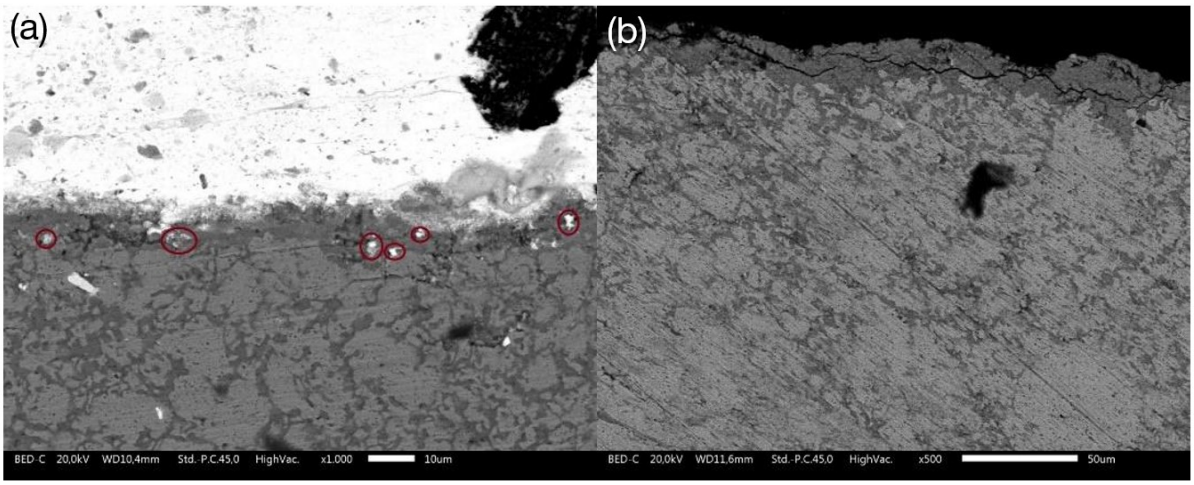

Figure 13. Average SEM Results ODS A (a) 1000× (b) 500×

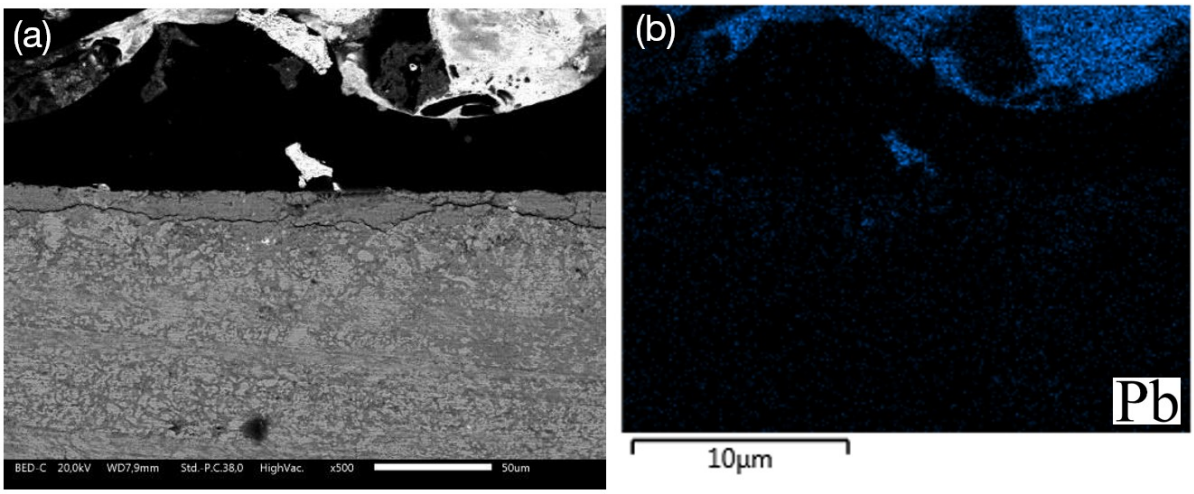

Figure 14. SEM Results ODS C (a) 500× (b) 500× with Pb Mapping

the depth range of 12.1 μm to 17.4 μm, likely consists of FeCr, as indicated by the high levels of Fe and Cr in this range. The boundary between the FeCr layer and the substrate is marked by a significant increase in Fe content, indicating the start of the substrate layer at a depth of 17.8 μm. Figure 8c also demonstrates the types of layers formed in Sample ODS C.

The final protective oxide layer is characterized by chromium enrichment. Oxidation involves the outward diffusion of iron cations through the oxide layer from the bulk diffusion zone, while oxygen diffuses inward through the oxide layer into the diffusion zone. The interface between the iron oxide/spinel layer continuously moves inward. Using this physical model and understanding the diffusion behavior of the elements, we can predict the concentrations of Fe, Cr, and O in each layer. Oxygen is expected to have the highest concentration in the oxide layer, decreasing to zero after passing through the diffusion zone. Chromium is likely to be minimal in the outer layer, reaching its maximum concentration in the spinel layer before returning to the bulk alloy concentration. Meanwhile, iron is believed to dominate the outer layer, but its concentration reduces in the spinel layer and the diffusion zone before returning to its bulk alloy concentration. Refer to Figure 11 for an illustration.

The SEM results show the formation of oxide layers on each sample variation. The oxide thickness was measured by taking thickness measurements at multiple points on the samples and calculating the average oxide thickness for each variation. The following graph illustrates the average oxide thickness for each sample variation from Table 3 and Figure 12. The average values and error bars for each sample variation can be observed. ODS A has the smallest average oxide thickness compared to the other two samples. Despite having a similar composition to ODS B, where both samples use a single oxide in their composition, the oxide thickness results are significantly different. This discrepancy is due to the differences in the material struc-

ture resulting from the corrosion test conditions. The synthesis process of ODS A yielded a structure markedly different from the other samples, impacting the corrosion resistance results, particularly in terms of oxide thickness.

When comparing the average oxide thickness between Sample ODS B and ODS C, which were tested under identical environmental conditions, it is evident that Sample ODS C has a thinner oxide layer than ODS B. The key difference between these samples is the use of oxides in their composition. ODS C incorporates two oxides, Y_2O_3 and ZrO_2, whereas ODS B only uses ZrO2.

The use of two oxides demonstrates a significant impact, as the addition of Y_2O_3 to ODS steel enhances the material's oxidation resistance and phase stability at high temperatures (Zhu et al., 2023). This is evidenced by the SEM results showing that ODS C has higher oxidation resistance compared to ODS B, as indicated by the thinner oxide layer. Additionally, the oxide layer on ODS C is more uniform, suggesting that the addition of Y_2O_3 improves the material's stability at high temperatures. Comparing ODS C with ODS A in Table 3 reveals that ODS A has a thinner oxide layer than ODS C. However, the stability of ODS A is lower compared to Sample ODS C, as indicated by the higher inconsistency in oxide thickness in ODS A. This is quantitatively demonstrated in Table 3, where the standard deviation for ODS A is significantly higher than that for ODS C. This reinforces the assertion that the addition of Y_2O_3 has a substantial impact on the material's stability at high temperatures. All three samples were tested under identical temperature and duration conditions. Corrosion resistance analysis is based on SEM EDX results. Figure 13a shows the SEM results for ODS A. Pb penetration is observed in the oxide layer formed on ODS A. Additionally, some Pb points are seen in the substrate layer, likely residual from the corrosion test. Pb penetration typically starts from the outermost surface, so the presence of Pb in the substrate should correspond with significant penetration points on the surface (Jiang et al., 2022).

Despite the Pb penetration in the oxide layer, no Pb penetration is detected in the substrate layer of ODS A, indicating that the oxide layer effectively protects the material from Pb corrosion at 550°C for 75 hours. Figure 14a. presents the SEM results for ODS C at 500× magnification. The results show no Pb penetration in either the oxide surface or the substrate layer. A thin oxide layer forms on the material surface, enhancing its corrosion resistance in a Pb environment. However, the SEM results indicate inconsistency in the oxide layer thickness, with areas of both thin and thick oxide layers. Figure 14a displays the SEM results for ODS C at 500× magnification. There is no visible Pb penetration in either the oxide layer or the substrate layer. Some white spots are observed in the substrate layer, but these are not Pb penetration points. EDX results confirm that these white spots are not Pb. Figure 14b. shows that Pb is only present outside the oxide layer formed on the material's surface.

The XRD spectra for each sample indicate differences in oxide layer composition. The absence of secondary oxide phases such as ZrO_2 or Y_2O_3 in the XRD spectra suggests that these oxides remain finely dispersed within the matrix rather than forming separate crystalline phases detectable by conventional XRD. This supports the hypothesis that dispersed Y_2O_3 and ZrO_2 function as stabilizing agents rather than primary oxidation products, thereby facilitating the development of a dense and adherent Fe-Cr oxide layer (Wafda et al., 2024).

A comparison of the XRD patterns between ODS A, ODS B, and ODS C highlights how oxide composition influences oxidation resistance. ODS C, which incorporates both Y_2O_3 and ZrO_2, exhibits a more uniform and thinner oxide layer, as evidenced by the relatively lower intensity of Fe_2O_3 peaks in its XRD spectrum. This indicates enhanced oxidation resistance due to improved phase stability. Meanwhile, ODS B, which contains only ZrO_2, shows a slightly thicker oxide layer, reflecting its lower oxidation resistance compared to ODS C. ODS A, despite having a similar single-oxide composition to ODS B, exhibits significant variation in oxide thickness, likely due to differences in synthesis and microstructural characteristics.

Additionally, the correlation between the XRD findings and SEM-EDX results further supports the role of oxide dispersoids in oxidation resistance. The thinner oxide layer observed in ODS C corresponds to the lower Fe_2O_3 peak intensity in its XRD spectrum, reinforcing the conclusion that Y_2O_3 contributes to stabilizing the oxide layer. This is further supported by previous studies Jiang et al. (2022), which indicate that Y_2O_3 addition enhances oxidation resistance and improves phase stability at elevated temperatures.

4. CONCLUSIONS

This study demonstrates that the addition of Y_2O_3 and ZrO_2 significantly enhances the microstructure and corrosion resistance of 9Cr ODS steels in high-temperature lead environments. Microstructural analysis revealed a ferritic matrix with finer grains enhancing hardness and oxidation resistance. Corrosion testing at 550°C for 75 hours indicated that ODS C ($Y_2O_3 + ZrO_2$) formed the most uniform protective oxide layer, effectively preventing Pb penetration. The improved resistance was attributed to Fe_3O_4 and Fe-Cr spinel formation, though residual porosity in some samples highlighted the need for synthesis optimization. The study highlights that oxide dispersion stabilizes the oxide layer, enhancing corrosion resistance under extreme conditions. Further research on long-term Pb exposure, microstructural optimization, and alloying additions is needed. These findings support the potential of ODS steels for LFR structural applications, pending validation under reactor conditions.

5. ACKNOWLEDGEMENT

The authors express their gratitude to BRIN and ITB for their support in carrying out this research. This research was financially supported by the Lembaga Pengelola Dana Pendidikan (LPDP) from the Ministry of Finance – Republic of Indonesia through Riset dan Inovasi untuk Indonesia Maju (RIIM)

Batch 3 with grant number B-848/II.7.5/FR.06/5/2023, ITB research program grant number 324H/IT 1.C02/KU/2023 and Rumah Program Hasil Inovasi Teknologi Nuklir 2025.

REFERENCES

Alemberti, A. (2016). The Lead Fast Reactor: An Opportunity for the Future? *Engineering*, **2**(1); 59–62

Bari, B. E. and D. Irwanto (2021). Wall Effect Analysis in Thermal-Hydraulics Aspect of HTR-10 and PR-3000 Reactors Using Different Porosity Models. *Science and Technology Indonesia*, **6**(4); 235–241

Bassini, S., S. Cataldo, C. Cristalli, A. Fiore, C. Sartorio, M. Tarantino, and M. Frignani (2020). Material Performance in Lead and Lead-Bismuth Alloy. In *Comprehensive Nuclear Materials: Second Edition*. Elsevier, pages 218–241

Chen, L., M. Wang, V. Tsisar, C. Schroer, and Z. Zhou (2020). Investigation of Microstructure and Liquid Pb Corrosion Behavior of a Fe-18Ni-16Cr-4Al Base Alumina-Forming Austenitic Stainless Steel. *Materials Research Express*, **7**(2); 026533

Del Giacco, M., A. Weisenburger, P. Spieler, F. Zimmermann, F. Lang, A. Jianu, and G. Mueller (2012). Experimental Equipment for Fretting Corrosion Simulation in Heavy Liquid Metals for Nuclear Applications. *Wear*, **280–281**; 46–53

Dömstedt, P., M. Lundberg, and P. Szakalos (2019). Corrosion Studies of Low-Alloyed FeCrAl Steels in Liquid Pb at 750 °C. *Oxidation of Metals*, **91**(3); 511–524

Giuranno, D., S. Amore, R. Novakovic, C. Tomasi, and E. Ricci (2021). Wetting Property of Liquid Pb on Different Steel Candidates as Structural Materials for the Generation IV Nuclear Reactors. *High Temperatures - High Pressures*, **50**(1); 49–61

Gong, X., M. P. Short, T. Auger, E. Charalampopoulou, and K. Lambrinou (2022). Environmental Degradation of Structural Materials in Liquid Pb- and Pb-Bi Eutectic-Cooled Reactors. *Progress in Materials Science*, **126**; 100920

Henry, J. and S. A. Maloy (2017). Irradiation-Resistant Ferritic and Martensitic Steels as Core Materials for Generation IV Nuclear Reactors. In *Structural Materials for Generation IV Nuclear Reactors*. pages 329–355

Jiang, H., X. Zhao, D. Wang, Q. Zhu, T. Li, and Y. Lei (2022). Effects of Y_2O_3 Addition on the Microstructure and Static Pb-Bi Eutectic Thermal Corrosion Behaviors of FeCrAlTiC-xY_2O_3 Laser Clade Coatings. *Coatings*, **12**(11); 1759

Kimura, A., W. Han, H. Je, K. Yabuuchi, and R. Kasada (2016). Oxide Dispersion Strengthened Steels for Advanced Blanket Systems. *Plasma and Fusion Research*, **11**(1); 2505090–2505090

Lorusso, P., S. Bassini, A. Del Nevo, I. Di Piazza, F. Giannetti, M. Tarantino, and M. Utili (2018). GEN-IV LFR Development: Status & Perspectives. *Progress in Nuclear Energy*, **105**; 318–331

Martinelli, L., K. Ginestar, V. Botton, C. Delisle, and F. Balbaud-Célérier (2020). Corrosion of T91 and Pure Iron in Flowing and Static Pb-Bi Alloy Between 450 °C and 540 °C: Experiments, Modelling and Mechanism. *Corrosion Science*, **176**; 108897

Navas, M. and R. Hernández (2018). Compatibility of Structural Materials with Lead and Lead Bismuth Eutectic for CSP Applications. In *AIP Conference Proceedings*, volume 2033. American Institute of Physics Inc.

Parida, P. K., A. Dasgupta, S. Bajpai, T. Sakthivel, and R. Mythili (2023). Synthesis and Characterization of 9Cr ODS F/M Steel with Optimized Y_2O_3 and Ti Content and Its Comparison with P91 Steel. *Powder Technology*, **425**; 118564

Ricci, E., D. Giuranno, G. Canu, S. Amore, and R. Novakovic (2018). Corrosion Behaviour of Oxide Dispersion Strengthened Iron-Chromium Steels in Liquid Pb at 973 K. *Materials and Corrosion*, **69**(11); 1584–1596

Tsisar, V. and O. Yeliseyeva (2007). Oxidation of Armco-Fe and Steels in Oxygen-Saturated Liquid Pb. *Materials at High Temperatures*, **24**(2); 93–101

Wafda, H., D. H. Prajitno, E. A. Basuki, A. Syafiq, N. Widiawati, and A. P. A. Mustari (2024). High Temperature Oxidation Behavior of ODS Ferritic Stainless Steel Fe-16Cr-4Al-1Ni-0.4Y_2O_3. *Indonesian Journal of Chemistry*, **24**(5); 1456–1469

Wafda, H., F. Roswita, D. H. Prajitno, and A. P. A. Mustari (2023). New Alloy Synthesis of Oxide Dispersion Strengthened (ODS) Ferritic Steel Fe-Cr-Al-W-Ti-Zr with Y_2O_3 Dispersoid as a Candidate Fuel Cladding Material for Nuclear Reactors Using Mechanosynthesis Method. *Jurnal Iptek Nuklir Ganendra*, **26**(2); 72–81

Wang, G., Z. Wang, and D. Yun (2023). Cladding Failure Modelling for Lead-Based Fast Reactors: A Review and Prospects. *Metals*, **13**(9); 1524

Wang, H., J. Xiao, H. Wang, Y. Chen, X. Yin, and N. Guo (2021a). Corrosion Behavior and Surface Treatment of Cladding Materials Used in High-Temperature Lead-Bismuth Eutectic Alloy: A Review. *Coatings*, **11**(3); 1524

Wang, J., S. Liu, B. Xu, J. Zhang, M. Sun, and D. Li (2021b). Research Progress on Preparation Technology of Oxide Dispersion Strengthened Steel for Nuclear Energy. *International Journal of Extreme Manufacturing*, **3**(3); 032001

Xiao, Z., J. Liu, Z. Jiang, and L. Luo (2022). Corrosion Behavior of Refractory Metals in Liquid Pb at 1000 °C for 1000 h. *Nuclear Engineering and Technology*, **54**(6); 1954–1961

Yaskiv, O. I. and V. M. Fedirko (2014). Oxidation/Corrosion Behaviour of ODS Ferritic/Martensitic Steels in Pb Melt at Elevated Temperature. *International Journal of Nuclear Energy*, **2014**(1); 657689

Zhu, C., W. Zhang, M. Zhou, L. Lv, Y. Zhong, Q. Li, and J. Yang (2023). Effect of Y_2O_3 Content on Microstructure and Corrosion Behavior of ZrO_2 Coatings in Liquid Lead-Bismuth Eutectic. *Materials Chemistry and Physics*, **309**; 128392

Zinkle, S. J., J. L. Boutard, D. T. Hoelzer, A. Kimura, R. Lindau, G. R. Odette, and H. Tanigawa (2017). Development of Next Generation Tempered and ODS Reduced Activation

Ferritic/Martensitic Steels for Fusion Energy Applications. *Nuclear Fusion*, **57**(9); 092005

Şahin, S. and Y. Wu (2018). 3.14 Fission Energy Production. In *Comprehensive Energy Systems: Volumes 1–5*, volume 3. pages 590–637